IET Radar, Sonar & Navigation

WILEY

The Institution of Engineering and Technology

ORIGINAL RESEARCH OPEN ACCESS

A Flexible K-Band FMCW Radar Prototype for Low-RCS Nano-Drone Detection

Safiah Zulkifli[1,2] | Alessio Balleri[2]

[1]School of Aerospace Engineering, Universiti Sains Malaysia, Engineering Campus, Pulau Pinang, Malaysia | [2]Centre for Defence Engineering and Physical Science, Cranfield University, Defence Academy of the UK, Shrivenham, UK

Correspondence: Alessio Balleri (a.balleri@cranfield.ac.uk)

Received: 7 April 2025 | **Revised:** 25 July 2025 | **Accepted:** 4 August 2025

Handling Editor: Francesco Picariello

Funding: The authors received no specific funding for this work.

Keywords: FM radar | micro-Doppler | radar detection

ABSTRACT

Nano-drones are insect-like drones used to provide intelligence through their capability of intrusion and ability to carry small sensors. They pose a defence and security threat and can potentially violate secure establishments and privacy rights. Their rapid emergence and increased availability have made them an existing technology which is affordable and easy to operate. Nano-drones are typically defined as drones smaller than 15 cm. They are light and stealthy in nature and present a very low radar cross-section (RCS) which creates a significant challenge for active Radio Frequency (RF) security systems tasked with detecting potential threats. This paper presents a K-band Frequency Modulated Continuous Wave (FMCW) radar prototype tailored for detecting nano-drones. Operating at 24 GHz and utilising commercial off-the-shelf components, the radar offers a low-cost, flexible and customisable solution with user-selectable frequency and waveform parameters. The system's detection capabilities were tested using low-RCS oscillating metallic spheres ranging from 0.5 to 3.0 cm in diameter. Nano-drone detection was demonstrated using range-Doppler maps and time-frequency spectrograms of a real and small 5 cm nano-drone. The paper provides a detailed overview of the radar design and test methodology, together with a detailed investigation of the radar performance.

1 | Introduction

The surge in nano-drone technology, unmanned aerial vehicles (UAV) often smaller than 15 cm, has introduced new security challenges. Drones are increasingly agile, affordable, adaptable, accessible, and anonymous [1]. Although these qualities enable legitimate applications, they also make nano-drones highly susceptible to misuse. Equipped with high-resolution cameras, miniature microphones, and advanced sensors, these drones can perform covert surveillance and other potentially malicious activities. One notable example is the Black Hornet nano-drone, which has been deployed in military operations for reconnaissance, allowing operators to scan enemy territories from a safe distance [2]. Leveraging remote technology, the drone operator can be anonymous and sheltered.

Detecting small and nano-sized drones remains a major challenge for radar-based surveillance systems due to their extremely low radar cross-section (RCS), which often makes them nearly invisible to conventional radar technologies. These drones, typically built with lightweight plastic materials, exhibit minimal radar reflectivity, frequently with RCS values below 0.01 m^2 (-20 dBm^2) [3–6]. Although a substantial body of work has explored the detection of micro-drones, and most efforts focus on

This is an open access article under the terms of the Creative Commons Attribution License, which permits use, distribution and reproduction in any medium, provided the original work is properly cited.

© 2025 The Author(s). *IET Radar, Sonar & Navigation* published by John Wiley & Sons Ltd on behalf of The Institution of Engineering and Technology.

targets with physical dimensions and RCS levels comparable to birds, very few studies have addressed the detection or RCS measurements of drones with diagonal sizes under 15 cm. A notable exception is the work in ref. [7], which provided the first three-dimensional RCS measurements of a nano-drone at K-band (24 GHz), revealing values as low as -55 dBm^2 depending on aspect and elevation angles. This lack of literature highlights the need for specialised detection systems tailored to such low-RCS targets. Frequency Modulated Continuous Wave (FMCW) radar offers a promising solution, particularly due to its advantages in short-range detection, low power consumption, compact hardware, and ability to mitigate blind zones. These features make FMCW radar especially suitable for detecting nano-drones, filling a critical gap left unaddressed by conventional radar approaches focused on larger UAVs.

In an analysis of drone detection using the FEKO simulation software, an OktoXL Mikrokopter was modelled and analysed for rotational propeller speeds between 2000 and 5000 rev/min [8]. The authors demonstrated that aliasing could occur easily due to the high speed of the propellers. Experimental-based investigations using software-defined radio (SDR) platforms have also been employed for drone detection. In ref. [9], for example, the authors used different operating frequencies and different types of waveforms to detect drones using a radar prototype based on an SDR. The study in ref. [10] compared the detection performance of a software-defined radio (SDR)-based radar system [11] with that of a custom-designed analogue radar prototype [12] for identifying a Xiro Xplorer drone. The findings indicated that the primary limitations associated with the SDR approach stemmed from hardware bandwidth constraints and relatively high equipment costs.

In refs. [13–15], the authors investigated the detection of a DJI Phantom Quadcopter with a 94 GHz FMCW radar. Both a scanning radar and a static multi-channel front-end radar were used. Because of the high operating frequency, the results confirmed a limited detection range, primarily due to high attenuation losses through the atmosphere. Similarly, a much lower operating frequency (35 GHz) was deployed [16] to detect two types of micro-drones; the DJI Phantom 2 and the DJI S1000 Premium. Results showed the manoeuvring drone induced a wide Doppler spread due to the rotating propeller blades, which can be useful for drone characterisation. On the other hand, Kyritsis et al. [17] demonstrate that K-band offers a good trade-off between resolution and range. Experimental results confirm its effectiveness in detecting various drone models, making it a viable solution for enhanced drone detection. Apart from that, a manufactured board with an X-band FMCW radar [18] was used to detect two flying DJI Phantom 2 drones within a flight range of 20–500 m. In another major study [19], authors replaced RF cables with fibre-optic links in a K-band FMCW in an attempt to reduce losses. With such solution, they managed to detect a BumbleBee F820 hexacopter within a range of 500 m. A drone at a much longer range of just over 1 km was detected and reported in ref. [20] with an X-band FMCW radar.

Alternative approaches, though slightly more complicated, have been proposed to detect drones. These explore phased arrays, digital arrays, digital beamforming, and multiple-input multiple-output (MIMO) radars. In refs. [21–23], an X-band receiver with a new dedicated antenna design was used to gather data of a DJI Phantom 4 drone up to a distance of 2 km [24, 25]. In ref. [26], the authors proposed a 60 GHz FMCW radar with two receiving antennas, rather than a phased array. A similar system is the MIMO FMCW radar described in ref. [27], which operates at 37.5 GHz and was developed by a consortium of Italian universities using GaN chips fabricated by OMMIC.

The micro-Doppler signatures of drones have also attracted considerable research efforts as a means to extract target characteristics and facilitate target classification. Authors in refs. [28–31] have all investigated and presented results relative to the distinct micro-Doppler signature of drones collected with X-band FMCW radars. The authors in ref. [32], on the other hand, compared signatures collected at K-band and at W-band with FMCW radar technology. By using an SDR, the authors in ref. [33] presented a comparison between four different frequency bands, all lower than 9 GHz.

A summary of the key drone targets that have been studied in the existing literature is presented in Table 1. Despite the vast amount of previous research available on radar detection of drones, to the best of our knowledge, very few, if any, have investigated the use of dedicated radar to detect nano-drones, particularly those smaller than 15 cm as investigated here. In this paper, we present a K-band FMCW radar prototype designed to examine the detection of low RCS nano-targets. The radar has already been introduced in refs. [34, 35]. Here it is presented in much more detail, along with new experimental results that demonstrate its performance against short-range low-RCS targets. In contrast to available off-the-shelf integrated radar, this prototype offers wide flexibility in the selection of the radar parameters that include the tuning of the exact operating frequency, and a selection of the ramp bandwidth, ramp duration, waveform design, and integration time on the target. This enables the user to select the best parameters according to the performance required against such small targets. The performance of the prototype was validated through a series of experimental trials involving metallic bearing spheres and a commercial Arcade small nano-drone with an approximate body size of 15 cm. The results confirm that the radar is capable of detecting extremely small targets and analysing their return signatures, offering valuable insights into the presence and behaviour of the targets.

The remainder of this paper is organised as follows. Section 2 outlines the design of the radar system, encompassing both the hardware implementation and the signal processing framework. Section 3 presents a thorough performance evaluation through three experimental scenarios: (i) detection of a single metallic sphere, (ii) detection of multiple metallic spheres and (iii) detection of a commercial nano-drone. Finally, Section 4 summarises the key findings and outlines future directions.

2 | Radar Design Model

This section presents the received signal model for the FMCW radar and outlines the architecture of the developed prototype. The design prioritises cost-effectiveness and component minimisation, emphasising affordability and simplicity. To this end, a

TABLE 1 | Summary of related work on drone detection using CW or FMCW radar.

Refs	Details of the radar system	Target model and its size	
[8]	24 GHz FMCW radar (from IMST GmbH)	OktoXL Mikrokopter	Propeller: 30.5 cm
[10]	Digital C-band FMCW versus Analog FMCW versus CW noise radar	Xiro Xplorer Drone	31 × 31 × 5.5 cm
[13–15]	94 GHz (W-band) FMCW radar [DDS chip + LO + Optical camera]	DJI Phantom	Diagonal length: 35 cm
[16]	35 GHz FMCW radar. Analogue front-end + pre-processing FPGA board + based processing PC	DJI Phantom 2	Diagonal length: 35 cm
		DJI S1000 Premium	51.1 × 45.5 × 29.5 cm
[19]	24.59 GHz (K-band) FMCW radar based on fibre-optic links	HexacopterBumbleBee F820	82 × 82 × 44 cm diameter propeller: 38 cm
[24, 25]	8.75 GHz (X-band) FMCW radar, RAD-DAR digital array radar	DJI Phantom 4	Diagonal length: 35 cm
[29]	X-band CW radar (9.7 GHz)	YAK54 Plane	Wingspan: 8.16 m
		EasyStar El-Sailor Plane	Wingspan: 2 m
		Mikado Logo 700	Propeller: 75 cm
		Mikado Logo 400	Propeller: 104 cm
		Align T-REX 450	Propeller: 71.5 cm
		Parrot AR. Drone	Propeller: 20 cm
		Stationary Rotors	Propeller: 20.3 cm
[32]	K-band (24 GHz) and W-band (94 GHz) FMCW radar	DJI Phantom 3 Standard	Blade length 13 cm
		DJI INSPIRE 1	Blade length 34.5 cm
		DJI S900 Hexacopter	Blade length 38.1 cm
		Northern Hawk Owl	Wingspan: 45 cm
		Harris Hawk	Wingspan: 115 cm
		Indian Eagle Owl	Wingspan: 135 cm
		Tawny Eagle	Wingspan: 175 cm
[33]	3.5, 4.5, 6 and 9 GHz FMCW waveforms radar Programed	DJI Phantom	Propeller: 24 cm
		DJI Mavic Pro	Propeller: 21 cm
		DJI Mavic Air	Propeller: 13.5 cm

conventional IQ demodulation scheme was deliberately omitted in favour of a single-channel mixer followed by intermediate frequency (IF) processing. This approach significantly reduced hardware complexity and cost while maintaining satisfactory radar performance. The limitation of this solution, as shown in the following paragraphs, is the introduction of a small blind range. A detailed discussion is presented in this section.

Let us consider an FMCW radar system that transmits a linearly frequency modulated ramp of duration T_r over a frequency bandwidth B. The ramp slope is defined as $\gamma = B/T_r$ and the one-ramp signal can be represented as follows:

$$S_T(t) = \cos\left(2\pi f_0 t + \gamma\pi t^2\right), \tag{1}$$

with a carrier frequency f_0. The received signal from a stationary target at a range R_0 can be expressed as follows:

$$S_R(t) = \cos\left(2\pi f_0 (t - t_0) + \gamma\pi (t - t_0)^2\right), \tag{2}$$

with a time delay $t_0 = 2R_0/c$ which depends on the target range R_0 and the speed of propagation of light c. The received signal is mixed with a copy of the transmitted signal as

$$S_{f_b}(t) = S_T(t) \times S_R(t), \tag{3}$$

to obtain the signal

$$\begin{aligned} S_{f_b}(t) = &\cos\left(2\pi f_o t_o + 2\pi\gamma t_o t - \pi\gamma {t_o}^2\right) \\ &+ \cos\left(4\pi f_o t + 2\pi\gamma t^2 - 2\pi f_o t_o - 2\pi\gamma t_o t + \pi\gamma {t_o}^2\right). \end{aligned} \tag{4}$$

The second term in Equation (4) is centred at double the carrier frequency f_o and is filtered out with the use of a low-pass filter. The instantaneous frequency of the resulting signal is called the beat frequency f_b and is simply the derivative of the phase of $\cos\left(2\pi f_o t_o + 2\pi\gamma t_o t - \pi\gamma {t_o}^2\right)$ which results in

$$f_b = \frac{1}{2\pi}\frac{d}{dt}\phi(t) = \gamma t_0, \tag{5}$$

The return signal after the mixer consists of a positive and a negative spectrum component which are centred at the positive and negative beat frequency

$$f_b = \gamma t_0 = \frac{B}{T_r} \cdot \frac{2R_0}{c}, \tag{6}$$

which is a function of the product between the chirp slope and the echo time delay. Equation (6) shows that there are three main parameters that will affect the position of the beat-frequency spectrum: the ramp duration, the frequency bandwidth, and the range of the target to the radar.

Decreasing the ramp duration will increase the beat signal frequency, that is, the spectrum centred at f_b will shift away from DC. However, a lower ramp duration also results in a shorter integration time that will increase the spectrum spread (which is inversely proportional to the ramp duration and equal to $1/T_r$). This degrades the filtering performance as the narrower the spectrum, the better the time resolution.

Increasing the ramp bandwidth increases the beat signal frequency, resulting in a wider separation between the positive and negative spectrum contributions. Using a large bandwidth mitigates frequency overlaps and provides a better range resolution $\Delta R = \frac{c}{2B}$. However, there might be limitations on the linearity of the chirp signal for large bandwidths.

The beat signal frequency also depends on the target range R_0. The closer the target, the lower the resulting beat signal frequency. The radar cannot detect the target efficiently once the distance of the target is below the radar range resolution, as the positive and negative spectrums will overlap. A blind range limitation is introduced where the minimum requirement for the radar to be effective is $R_0 > \frac{c}{2B}$. This limitation can be overcome by employing an IQ mixer, which inevitably results in higher costs.

2.1 | Prototype Implementation

The principal design consideration for the proposed radar prototype is to realise a low-cost, reconfigurable FMCW radar system that allows full user control over key operational parameters. This flexibility enables customisation of system performance according to specific application requirements. A linear ramp voltage is generated using a Keysight 33600A waveform generator (Figure 1) and applied to a Hittite HMC739LP4 voltage-controlled oscillator (VCO), implemented via an evaluation board comprising a monolithic microwave integrated circuit (MMIC). The VCO outputs a frequency-modulated signal within the K-band, serving as the radar's transmit waveform [36].

The output of the VCO is routed through a Mini-Circuits ZC2PD-18263-S+ power divider, which splits the signal into two paths. One path is directed to the transmit antenna, while the other is fed to the local oscillator (LO) port of a Marki Microwave MM1-1140HS double-balanced mixer to act as the reference for coherent demodulation. Target returns are captured by the receive antenna and amplified using an HD30172 low-noise amplifier (LNA) manufactured by HD Communications Corp. The amplified signal is then applied to the radio frequency (RF) port of the mixer, where it is heterodyned with the LO signal to produce an intermediate frequency (IF) signal. This IF signal is subsequently filtered using a Mini-Circuits VLF-45+ low-pass filter, with a nominal −3 dB bandwidth of 77 MHz, to remove high-frequency components before digitisation via a TiePie Handyscope HS5 USB oscilloscope. The overall RF architecture of the radar system is depicted in Figure 2.

The transmit and receive antennas are identical standard-gain horn antennas, with a gain of 18 dBi, a physical length of 135 mm, and an aperture of 40 mm × 50 mm. The corresponding measured −3 dB antenna beamwidths at 24 GHz are approximately 15° in both azimuth and elevation. The antennas were mounted side-by-side on a bracket, with the two aperture centres placed 8 cm apart, and 1.5 m above the ground. The bracket was built so that the orientation of the two antennas could be easily adjusted to allow measurements in co-polarisation (either HH or VV) and cross-polarisation.

The main advantage of this prototype is that it provides full control over the radar components and the flexibility to choose the radar parameters, thereby influencing the radar performance tailored to the specific application being considered. The operational frequency range of the HMC739LP4 VCO spans from 23.8 to 26.8 GHz, offering flexibility in selecting the frequency span and bandwidth. However, practical deployment requires that the sweep remain within the VCO's most linear operating region to maintain chirp fidelity and consistent radar performance. Based on the measured tuning response (i.e., output frequency vs. input voltage), the frequency sweep was confined to the relatively linear region corresponding to voltage inputs between approximately 1.0 and 3.5 V (Figure 3). This operating range was determined through empirical testing to minimise distortion in the IF signal and ensure the range

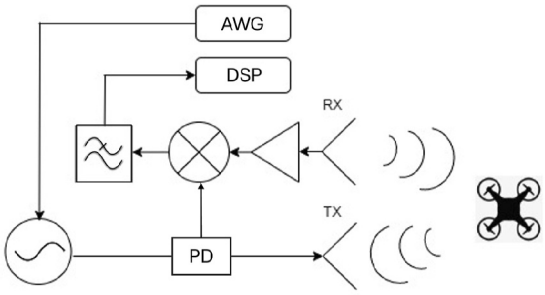


FIGURE 1 | Block diagram of K-band radar prototype.

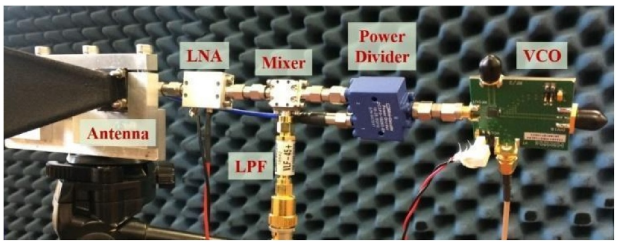


FIGURE 2 | A close-up of a K-band radar system developed.

response of the radar was a clean Sinc function with sidelobes at −13 dB. In this research, the tuning voltage (Vtune) was varied within the range of 1.1–1.5 V, corresponding to a frequency sweep from approximately 24.58–25.06 GHz.

2.2 | Signal Processing Steps

The raw intermediate frequency (IF) data acquired using the TiePie Handyscope HS5 digitiser is initially stored on a host computer for post-processing. Target detection and characterisation are performed through a structured sequence of signal processing operations, summarised as follows:

i. *Range Estimation*: A Fast Fourier Transform (FFT) is applied along the fast-time axis of the demodulated signal within time windows of duration T_r. This process yields a two-dimensional matrix representing signal intensity as a function of range and time, known as the Range-Time Intensity (RTI) matrix.

ii. *Doppler Processing*: A slow-time FFT is subsequently applied to each range bin of the RTI matrix to derive a Range-Doppler Map (RDM). This map provides a joint representation of target range and radial velocity, enabling the separation of moving targets from static clutter.

iii. *Time-Frequency Analysis*: To examine the temporal variation of spectral content within the identified target's range bin, a Short-Time Fourier Transform (STFT) is applied. The STFT is performed on the time-series signal extracted from the selected range bin in the RDM using nonoverlapping rectangular sliding windows. This operation produces a time-frequency spectrogram, enabling the observation of dynamic signal characteristics, such as periodic fluctuations or transient variations, which may reveal additional motion-related information about the target.

Although the current processing pipeline was implemented in an offline environment, the algorithmic structure, comprising sequential FFT operations and STFT, is inherently suitable for real-time implementation. By leveraging field-programmable gate arrays (FPGAs), embedded digital signal processors (DSPs), or real-time computing platforms, the system can be adapted to support live signal processing.

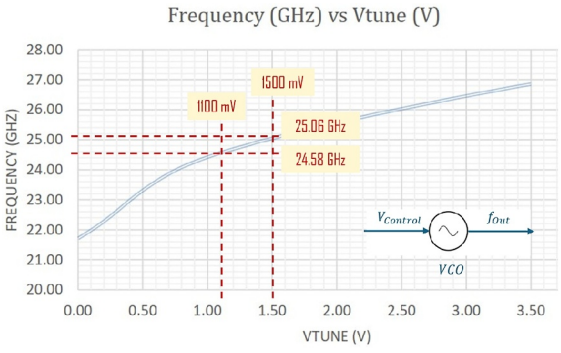


FIGURE 3 | Characteristic curve of the VCO.

3 | Performance Evaluation

All experiments presented here were conducted in the Radar Laboratory of Cranfield University, located at the Defence Academy of the UK in Shrivenham. The experimental trials were aimed at evaluating the detection performance of the radar prototype against small targets.

3.1 | Scenario A: Detection of Single Bearing Spheres

The main objective of these experimental trials was to demonstrate that the Doppler signature of very small bearing spheres could be detected with the developed prototype at the correct distance and with return level differences consistent with differences between their theoretical RCS. Five metallic spheres were measured with diameters equal to 30, 28.8, 19, 10 and 5 mm, respectively. A setup was constructed which consisted of two poles and a long horizontal fishing line to connect two opposite walls of the lab at a height of 216 cm. Each of the spheres was attached with adhesive tape to a vertical fishing line (approximately 65 cm long), with one extreme connected to the horizontal fishing line, and suspended to face the antennas 1.5 m above the ground floor and 3 m away from the radar (as shown in Figure 4). Linear Frequency Modulated (LFM) ramps, ranging from 24.58 to 25.06 GHz, were transmitted to achieve a range resolution of 31.25 cm. The ADC sampling frequency was set to 500 kHz and 1000 kSamples were collected to provide 2 s long recordings. Because the sampling frequency is much lower than the bandwidth of the low-pass filter, tests were carried out to establish the radar provided a response and a noise floor free

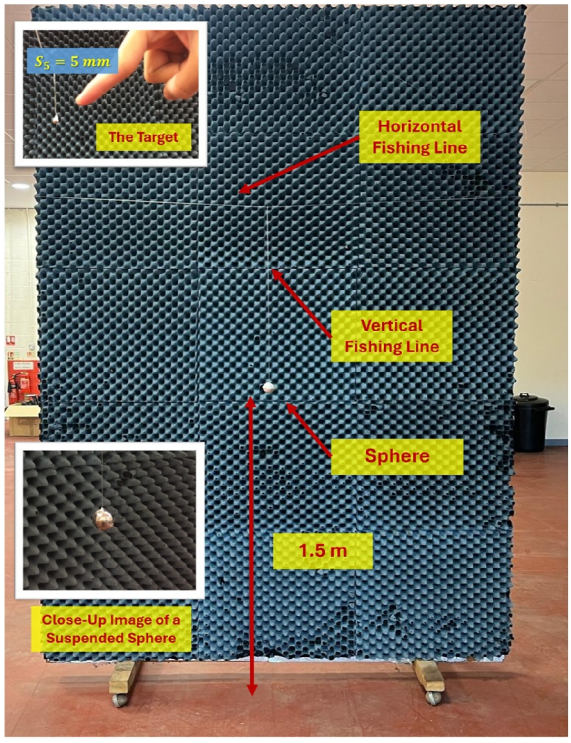


FIGURE 4 | Experimental arrangement showing the positioning of a single suspended sphere.

from aliasing at the range and Doppler intervals of interest. A summary of the radar parameter is provided in Table 2.

A Radar Absorbing Material (RAM) panel was placed behind the radar prototype and another one was placed 1 m behind the spheres. The RAM was used to reduce multipath contributions as the measurements were taken in an indoor confined space. Each sphere was subjected to two distinct motion patterns during the experiments: (i) radial oscillations along a front-to-back trajectory relative to the radar boresight and (ii) lateral oscillations perpendicular to the radar's line of sight. Notably, the smallest and lightest sphere (S_5) exhibited limited gravitational tension on the suspension line, resulting in reduced oscillatory motion. Consequently, S_5 predominantly hovered with an irregular trajectory during measurements. Table 3 provides the theoretical RCS values of the spheres in the Mie region calculated at 24.58 GHz, as in ref. [37].

3.1.1 | Radial Oscillations

Figure 5 presents the experimental radar returns from the five suspended metallic spheres undergoing radial oscillation, captured using both HH- and VV-polarised configurations. For each sphere and polarisation, corresponding RDMs and STFTs were generated. The amplitude data are shown in a non-calibrated dB scale.

TABLE 2 | Radar system parameters.

Arbitrary waveform generator (AWG)	Description
Shape	Sawtooth
Frequency	2 kHz
Amplitude	400 mV
Offset	1300 mV
	Values/units
Radar signal parameters	
Ramp duration	0.5 ms
Frequency 1	24.58 GHz
Frequency 2	25.06 GHz
Bandwidth	480 MHz
ADC parameters	
Sampling frequency	500 kHz
Number of samples	1000 kS

Because the exact trajectory of each sphere could not be controlled, to attempt and maintain a consistent, coherent integration gain between different spheres and measurements, and to allow fair amplitude comparisons, the RDMs were obtained with a short integration time of 60 ms (120 integrated ramps). The time-frequency analysis is presented for a longer time of 2 s over which the STFT was calculated with nonoverlapping sliding windows of 30 ms. In the plots, the frequency axis is oversampled by a factor of 16.

The RDMs are relative to specific collection times, and show spheres detected between 2.8 and 3.8 m away from the radar, although the extension of the oscillations may have been longer than this. This must be taken into account when analysing the results, as the strength of the sphere returns depends on both the size of the target (which determines its RCS values), target dynamics, and the distance from the radar. For example, with the same radar parameters and assuming the spheres remain within the main antenna beam during oscillation, an increase in the range between 2.5 and 3.5 m causes a target return drop of approximately 6 dB. These return drops are apparent in the time-frequency analysis showing 2 s long Doppler signatures.

The sidebands in the STFT are expected and they are simply due to the response of the rectangular sliding window. Sidelobes are expected every 1/30 ms (33.3 Hz) with the first sidelobe at −13 dB from the main peak.

A comparison between the two polarisations shows that, in the selected RDMs, the speed of the spheres in HH-pol was slightly lower than that in VV-pol and this resulted in Doppler migrations and overall higher integration gains in HH-pol.

The STFT analysis indicates the strongest return is for sphere S_1 in HH polarisation, with a peak power of 15.6 dB, whereas the weakest return was recorded for S_5 under VV polarisation at −4.4 dB. A similar pattern is reflected in the RDMs, where S_1 in HH polarisation again exhibits the highest return at 20.8 dB, and S_5 the lowest at 1.9 dB in VV polarisation. Among all tested spheres, S_5 showed the least different peak amplitude values between the two polarisations. A summary of the peak level returns is provided in Table 4.

When comparing theoretical RCS and measured amplitude peak level differences using the STFT results, the following results are observed:

- Between S_1 and S_5, the theoretical RCS difference is 10.6 dB, while the measured difference is 19.4 dB (HH) and 14.1 dB (VV).

TABLE 3 | Theoretical RCS of the spheres calculated at 24.58 GHz.

Sphere	Material	Diameter (mm)	RCS (m^2)	RCS (dBm^2)
S_1	Unknown metal	30.0	5.8039×10^{-4}	−32.4
S_2	Aluminium	28.8	7.0914×10^{-4}	−31.5
S_3	Aluminium	19.0	3.7755×10^{-4}	−34.2
S_4	Steel	10.0	1.1645×10^{-4}	−39.3
S_5	Steel	5.0	4.9978×10^{-5}	−43.0

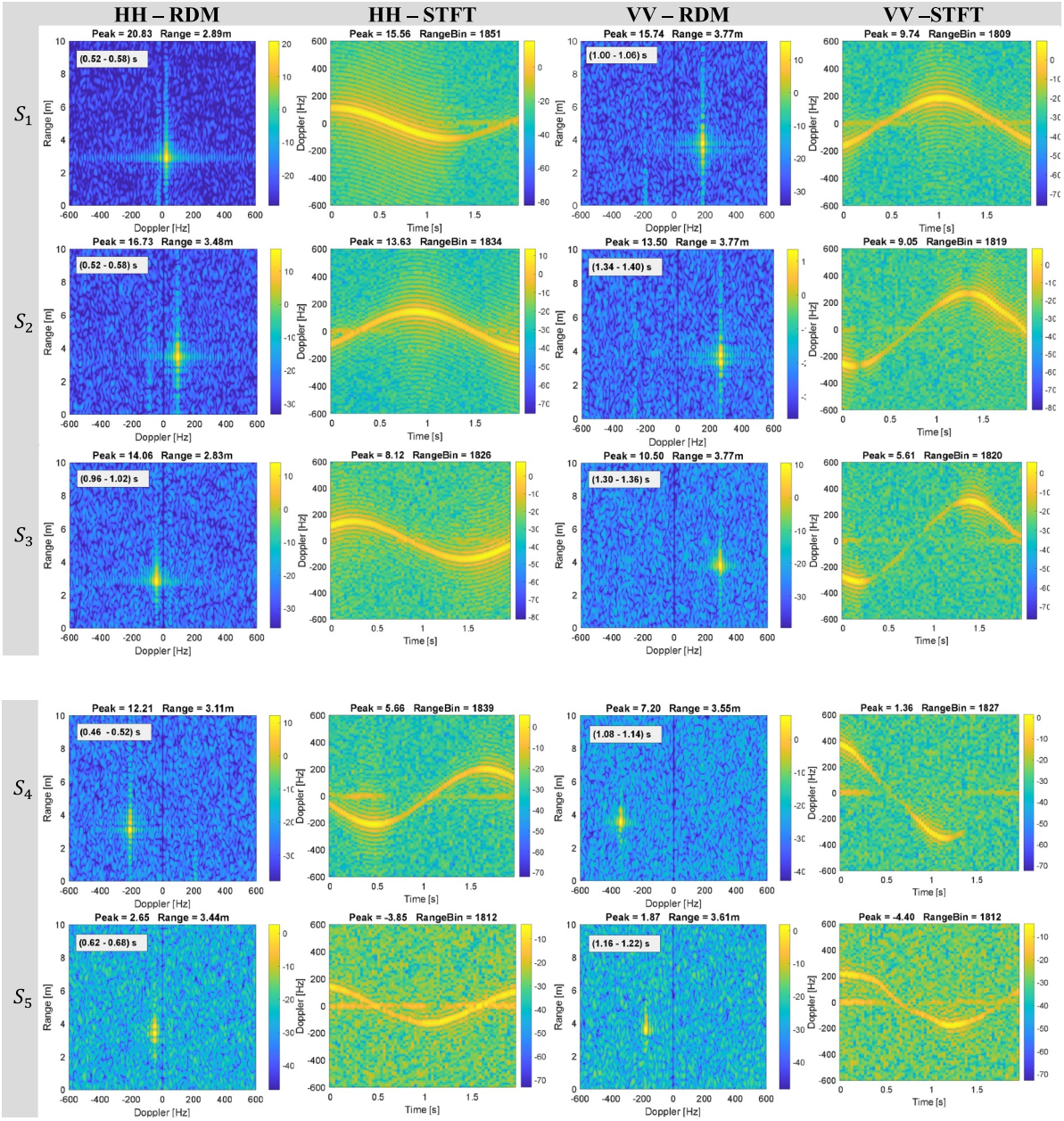


FIGURE 5 | Front-to-back oscillation with a window length of 30 ms for the STFT analysis.

- Between S_2 and S_5, the theoretical difference is 11.5 dB, with measured differences of 17.5 dB (HH) and 13.5 dB (VV).
- Between S_3 and S_5, the theoretical RCS offset is 8.8 dB, while measured values are 12 dB (HH) and 10 dB (VV).
- For S_4 versus S_5, the theoretical RCS difference is 3.7 dB, compared to measured values of 9.5 dB (HH) and 5.8 dB (VV).

The results of this analysis are summarised in Table 5. Each element in the table indicates the difference between the measured return offset and the theoretical RCS offset for each sphere pair.

3.1.2 | Lateral Oscillations

The results for the spheres oscillating perpendicular to radar boresight are presented in Figure 6. These were obtained with the same parameters used in the previous measurements, that is with 60 ms integration time for the RDMs and 30 ms long nonoverlapping windows to generate 2 s long micro-Doppler signatures. Unlike the previous case, the spheres moved between the main lobe and the side lobes of the antennas within an oscillation. At a range of 3 m the cross-range resolution is approximately 78 cm and the two antenna beams overlap by about 70 cm. Because of the lower radial velocities, the resulting Doppler shifts show a significant drop with respect to the previous experiment, and spheres were measured and detected at about 3 m away from the radar.

In this case, a 30-ms window length may be considered too long as within this integration time, the sphere no longer presents the same constant velocity vector. Differences in speed will result in noncoherent integration, causing variations in amplitude measurements between the HH-pol and the VV-pol.

Hence, from these tests, it is apparent that there are a few factors that will determine the retrieved amplitude values of a sphere: (i) the size of the sphere, (ii) the speed of the sphere and (iii) the aspect angle of the sphere.

The results obtained are summarised in Table 4. Differences in strength values can be compared with differences between the theoretical RCS values of the spheres in Table 3.

A quantitative comparison of measured versus theoretical RCS differences between S_1–S_5 and other sphere combinations is summarised as follows:

TABLE 4 | Summary of measured peak return levels from the experimental trials in dB (RDMs in black and STFT in red).

	Front-to-back oscillation (Figure 5)		Side-to-side oscillation (Figure 6)	
Target	**HH**	**VV**	**HH**	**VV**
Sphere S_1	20.8	15.7	16.0	15.2
	15.6	9.7	15.5	6.3
Sphere S_2	16.7	13.5	14.2	14.4
	13.6	9.1	14.0	9.2
Sphere S_3	14.1	10.5	12.4	8.7
	8.1	5.6	10.9	4.8
Sphere S_4	12.2	7.2	9.4	6.1
	5.7	1.4	5.8	1.6
Sphere S_5	2.7	1.9	3.1	1.0
	−3.9	−4.4	−2.3	−5.1

TABLE 5 | Summary of amplitude level analysis results using the STFT for the radial oscillations.

	S_1	S_2	S_3	S_4	S_5
HH					
S_1	0	2.8	5.6	3	8.8
S_2		0	2.8	0.2	6
S_3			0	−2.6	3.2
S_4				0	5.8
S_5					0
VV					
S_1	0	1.6	2.3	1.5	3.5
S_2		0	0.7	−0.1	2
S_3			0	−0.8	1.2
S_4				0	2.1
S_5					0

Note: Results indicate the difference in dB between the measured return offset and the theoretical RCS offset in dB.

- S_1 versus S_5: Theoretical RCS difference is 10.6 dB; measured differences are 17.8 dB (HH-pol) and 11.4 dB (VV-pol).
- S_2 versus S_5: Theoretical RCS difference is 11.5 dB; measured differences are 16.2 dB (HH-pol) and 14.3 dB (VV-pol).
- S_3 versus S_5: Theoretical RCS difference is 8.8 dB; measured differences are 13.1 dB (HH-pol) and 9.9 dB (VV-pol).
- S_4 versus S_5: Theoretical RCS difference is 3.7 dB; measured differences are 8 dB (HH-pol) and 6.7 dB (VV-pol).

These results, summarised in Table 6, indicate a generally consistent trend with theoretical expectations, though some discrepancies emerge due to differences in sphere dynamics and trajectory during measurements. The influence of oscillation speed on amplitude levels retrieval is particularly evident, highlighting the importance of motion-induced Doppler content in interpreting radar measurements.

It is apparent that all spheres were detected by the prototype with a good SNR at the correct range. The spheres used in the experiments are not targets calibrated for RCS measurements and therefore their actual RCS is not perfectly known. Although it is possible in dedicated facilities to achieve RCS measurement accuracies within 0.5 dB [38], our previous work using these spheres for RCS measurements in our lab, with much higher cost dedicated instrumentation such as a Vector Network Analyser (VNA), have shown the accuracy of this type of measurement is in worst cases within ± 2 dB [7]. With this in mind and considering all the other limitations around differences in dynamics and background contributions, the differences in levels obtained in this paper are overall consistent with what is expected from the theory.

3.2 | Scenario B: Detection of Multiple Bearing Spheres

A different experimental scenario was designed to evaluate the robustness of the developed radar prototype. This section aims to investigate the detection of multiple targets positioned in close proximity. In this setup, one sphere was placed at a distance of 2 m from the radar, while the second sphere was positioned 3 m away. The target arrangement is illustrated in Figure 7, where two targets, S_2 and S_3, were aligned within the radar's main beam line of sight. During the experiment, both spheres were released to swing simultaneously in the same direction. The experiment was conducted under four distinct configurations to evaluate the radar's performance under varying conditions:

i. HH polarisation with front-to-back oscillation (Figure 8)
ii. VV polarisation with front-to-back oscillation (Figure 9)
iii. HH polarisation with side-to-side oscillation (Figure 10)
iv. VV polarisation with side-to-side oscillation (Figure 11)

By varying the antenna polarisation and oscillation direction, these configurations were used to examine the radar's ability to

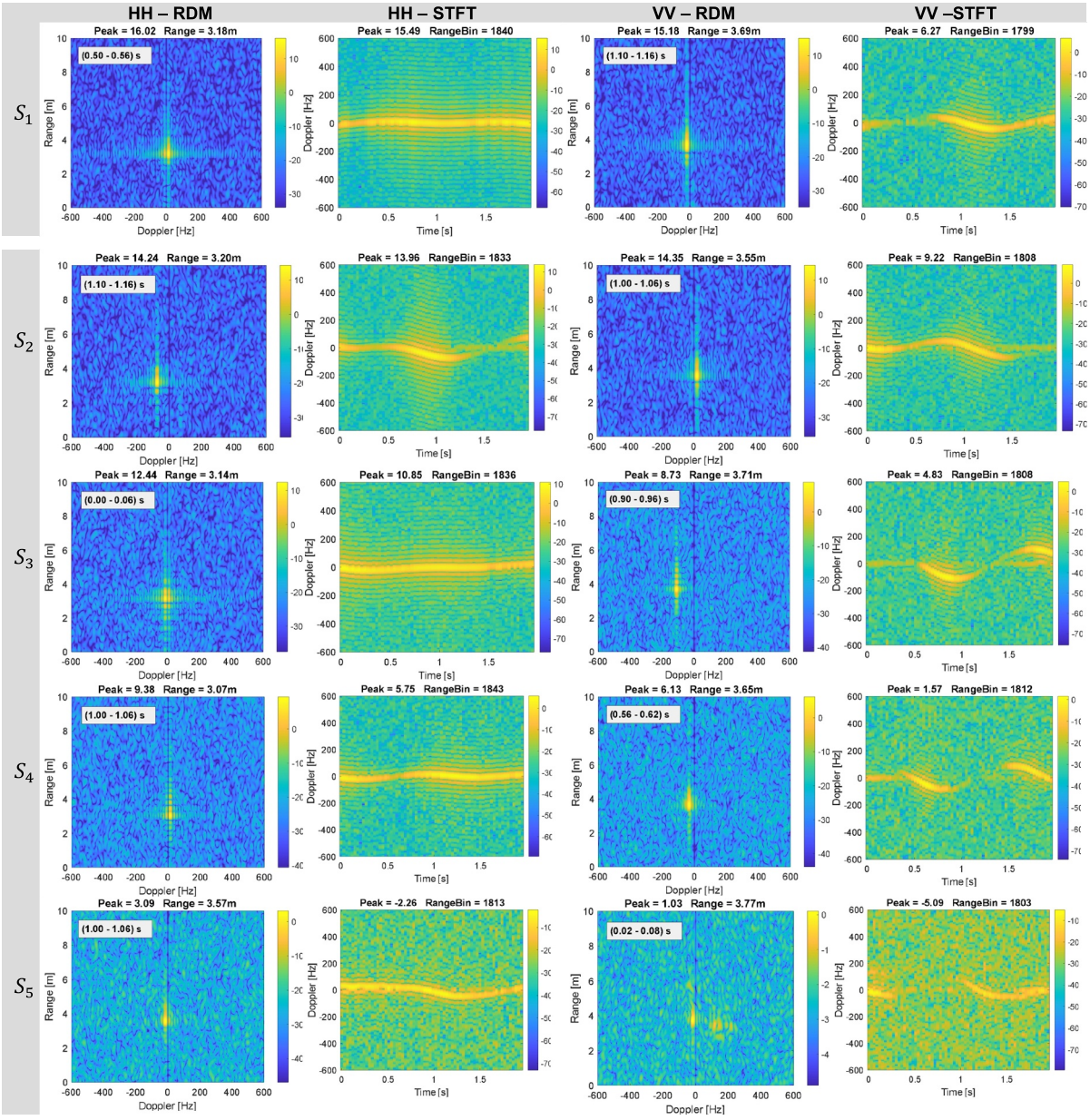


FIGURE 6 | Side-to-side oscillation with a window length of 30 ms for the STFT analysis.

distinguish multiple low-RCS targets at close range under different motion conditions.

A shorter integration time was utilised to maintain coherent integration, with 120 ramps of 0.5 ms ramp duration considered. Data were collected over a 2 s period for Doppler signature analysis. The RDM in Figure 8 displays two peaks corresponding to reflections from the two targets, located at distances of 3.1 and 4.5 m from the radar. Meanwhile, the STFT obtained with nonoverlapping 30 ms long windows illustrates the Doppler signature of both targets, showing an almost complete sinusoidal cycle within 2 s and indicating a rotational rate of approximately 0.5 Hz. The highest observed Doppler peak was at around 306 Hz, while another peak was recorded at 266 Hz. Both targets were moving in the same direction, although one appeared to lag behind the other by approximately 0.2–0.3 s. This delay may be attributed to the slightly greater weight of one target, affecting its velocity due to gravity during oscillation. Alternatively, the external force applied unevenly to the targets could have contributed to this discrepancy.

The polarisation was switched to VV, and the same experimental procedure was repeated. Figure 9 shows a RDM example with a target at 2.8 m approaching the radar, and the other at 4.1 m, moving away from the radar. The STFT in Figure 9 shows that both targets were oscillating in opposite directions. The highest Doppler frequency recorded for the fastest sphere was 400 Hz, while for the second sphere was 200 Hz. The highest peak returns from Figures 8 and 9 were 7.7 and 7.3 dB, respectively, and this is consistent with the theoretical expectation that the sphere RCS is the same in both co-polarisations.

Side-to-side oscillations with multiple targets were also measured for an evaluation. Figure 10a shows the RDM for the HH pol with

TABLE 6 | Summary of amplitude level analysis results using the STFT for the lateral oscillations.

	S_1	S_2	S_3	S_4	S_5
HH					
S_1	0	2.4	2.8	2.8	7.2
S_2		0	0.4	0.4	4.7
S_3			0	0	4.3
S_4				0	4.3
S_5					0
VV					
S_1	0	−2.1	−0.4	−2.2	0.8
S_2		0	1.7	−0.1	2.8
S_3			0	−1.8	1.1
S_4				0	3
S_5					0

Note: Results indicate the difference in dB between the measured return offset and the theoretical RCS offset in dB.

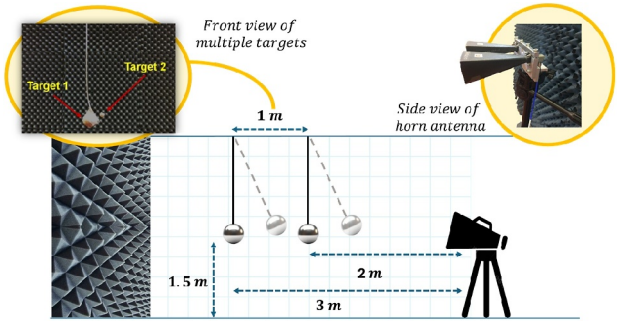


FIGURE 7 | Experimental arrangement of multiple bearing spheres. Target 1 is S_2 and Target 2 is S_3.

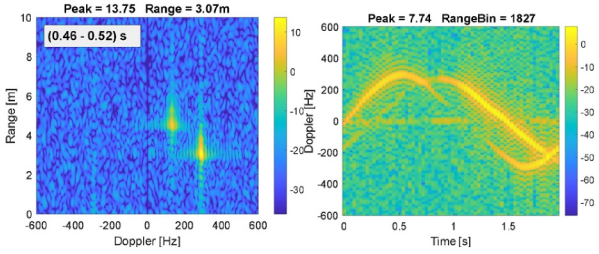


FIGURE 8 | Front-to-back oscillation of multiple targets in an HH-polarisation.

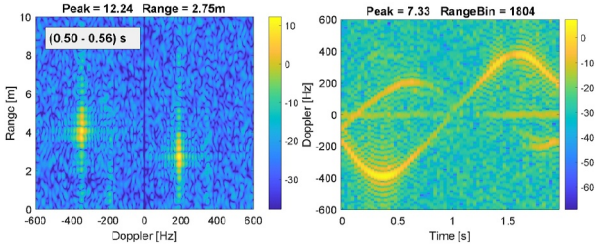


FIGURE 9 | Front-to-back oscillation of multiple targets in a VV-polarisation.

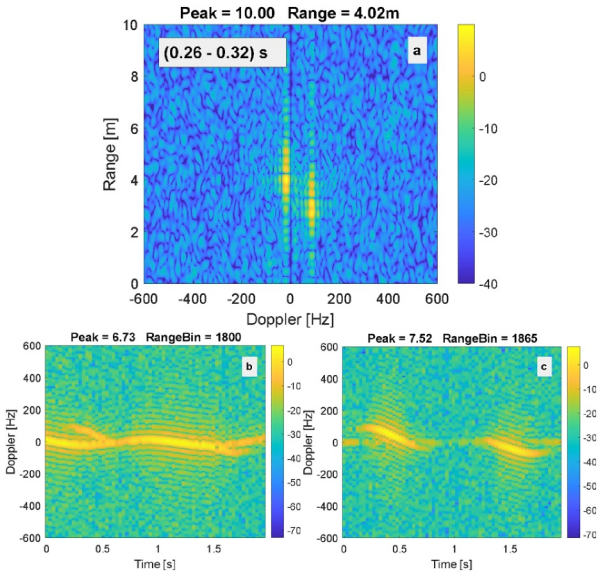


FIGURE 10 | Side-to-side oscillation of multiple targets in an HH-polarisation.

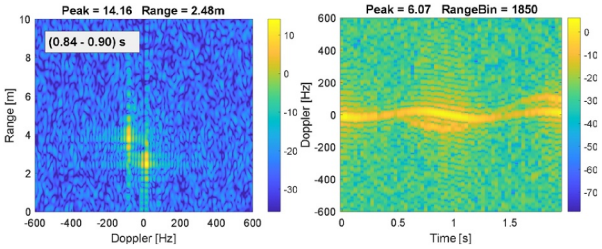


FIGURE 11 | Side-to-side oscillation of multiple targets in a VV-polarisation.

two peak responses, relative to one target at 4 m moving with a 23.3 Hz Doppler shift away from the radar, and another target at 3.1 m moving with a 88.3 Hz Doppler shift towards the radar. Figure 10b shows the micro-Doppler signature for the spheres at about 4 m, with a tip Doppler shift at 25 Hz. Within the dwell time of 2 s, the STFT shows about one and a half complete cycles, that is a rotational rate of approximately 0.75 Hz. Figure 10c shows the STFT of the second sphere extracted from the range bin at approximately 3 m. The maximum Doppler shift was 100 Hz, corresponding to a rotational rate of approximately 0.75 Hz. The stronger return from this sphere was 7.5 dB and a comparison to the highest return of the other sphere at 6.7 dB is in agreement with the expected theoretical RCS difference.

Figure 11 demonstrates that the radar prototype can resolve two spheres positioned at 2.4 and 3.8 m from the radar in VV polarisation. The RDM shows a target moving towards the radar with a 18.33 Hz Doppler shift and one moving away from the radar with a Doppler shift of 81.67 Hz. The two targets can be seen oscillating about zero Doppler in the STFT. The maximum Doppler tips achieved were 120 and 25 Hz, respectively, with a rotational rate of approximately 0.75 Hz. These findings show that, as for the previous test results, the radar could resolve targets as long as the separation between them was greater than the range and Doppler resolution of the radar.

3.3 | Scenario C: Detection of Nano-Drone

The last scenario demonstrated the detection of a real, small nano-drone target that is commercially available on the market. The target used in these experiments was an Arcade Pico Drone Nano Quadcopter, with a body size of approximately 15 cm (diagonal) and consisting of 4 propellers carrying 1.2 cm long blades as illustrated in Figure 12. RCS measurements of the Arcade Pico Drone were collected and presented in ref. [7].

The drone was tied up to a thin fishing line and suspended from the lab ceiling. The drone was also connected loosely to the floor to help it hover in one place and to minimise undefined trajectories. The drone was placed at antenna boresight and approximately 1.5 m above the ground, at the same height as the antennas. Figure 12b illustrates the hanging drone. Measurements were taken with the antennas in both HH-pol and VV-pol. Because the drone was attached to both top and bottom, it moved in a circular motion or pendulum-like motion during the measurements. This dynamic behaviour introduced varying radial velocity components of the drone body relative to the radar. Data were collected for 2 s time intervals. Tests were carried out to establish the radar provided a clean noise floor response with no moving targets in the scene.

Figure 13 shows a drone detection in HH-pol at a range of 3.96 m with a radial Doppler shift of approximately −146.7 Hz, indicating motion away from the radar. The STFT, obtained with 30 ms nonoverlapping rectangular windows, reveals a maximum Doppler of 183.5 Hz. The signature period of 2 s arises from the circular body motion of the suspended nano-drone.

In contrast, Figure 14 shows the signal return obtained in VV-polarisation. The drone remains detectable at the same range of 3.96 m at a lower Doppler shift of 21.67 Hz, indicating motion towards the radar. The observed maximum Doppler frequency in the STFT was approximately 112.3 Hz.

Further data were collected with a ramp duration of 250 μs and a sampling frequency of 1 MHz. Figure 15 shows the Doppler response of the nano-drone over a 2 s duration in HH-polarisation, obtained with 30 ms nonoverlapping windows. In this example, the central bright band around 0 Hz corresponds to the primary Doppler return from the body of the hanging nano-drone, which appears to be moving slowly or hovering with minimal radial velocity relative to the radar. Notably, additional spectral lines are observed over the main Doppler trace. These sideband features are indicative of periodic motion and their presence confirms the sensitivity of the prototype to detect the drone blades.

The spacing between these spectral lines can be used in future work to estimate the blade rotation rate, offering insight into the dynamic behaviour of the drone and drone type. Similar results for different types of manoeuvres, trajectories and for the drone in free flight were found and presented in [39].

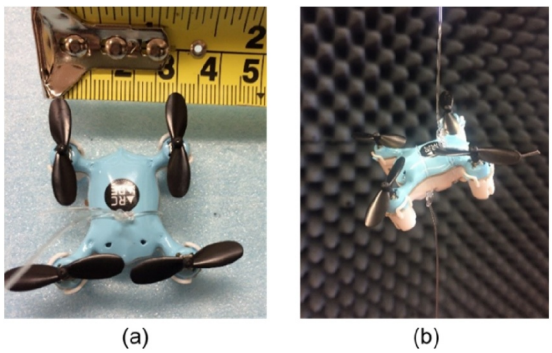


FIGURE 12 | (a) Close-up of ARCADE nano-drone and (b) the target hanging for data collection.

4 | Conclusion and Future Work

A flexible K-band FMCW radar prototype for detecting low-RCS targets has been developed and evaluated. Operating at approximately 24 GHz, the radar was designed with a low-cost architecture and enables adjustment of key parameters such as sweep bandwidth, duration, and operating frequency within the linear region of the VCO. The performance of the radar was assessed through experimental trials involving oscillating metallic spheres with diameters ranging from 0.5 to 3.0 cm (corresponding to RCS values between −32.4 and −43.0 dBm^2), as well as a 15 cm Arcade Pico Mini Pocket quadcopter. Successful detection of low-RCS targets was demonstrated, and the system was shown to resolve multiple closely spaced objects

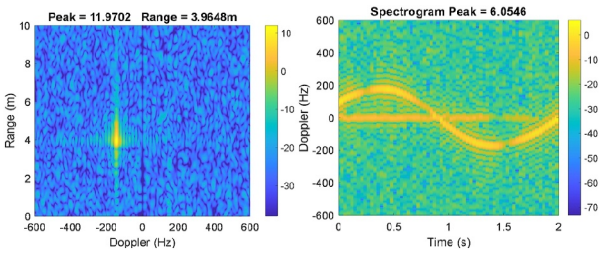


FIGURE 13 | HH-polarisation of a nano-drone response.

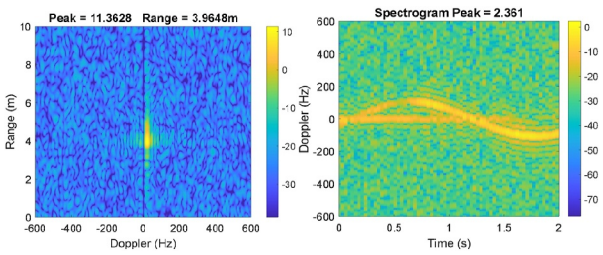


FIGURE 14 | VV-polarisation of a nano-drone response.

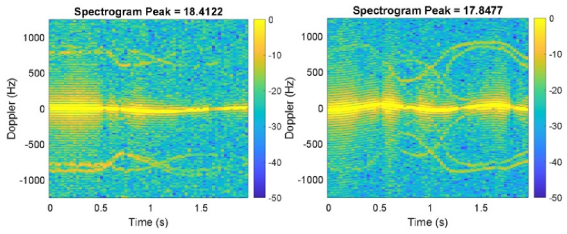


FIGURE 15 | Observed Jet engine modulation (JEM) features in the nano-drone Doppler return.

within its range resolution. Temporal variations in the return signals also provided informative signatures related to target motion.

Because of its compact size and effective short-range performance, the prototype may be suitable for other applications involving low-RCS objects, such as near-field insect tracking in entomological studies, where conventional radar systems are constrained by blind zones. Future work should investigate a broader range of nano-drone models with varying physical and dynamic characteristics. Additionally, the potential for incorporating signal classification techniques based on return signature features can be investigated to enhance target identification capability.

Author Contributions

Safiah Zulkifli: data curation, formal analysis, investigation, methodology, software, visualization, writing – original draft. **Alessio Balleri:** conceptualization, formal analysis, funding acquisition, investigation, methodology, project administration, resources, supervision, writing – review and editing.

Acknowledgements

The authors would like to thank the School of Aerospace Engineering, Universiti Sains Malaysia, Malaysia and the Malaysian Ministry of Higher Education for sponsoring the PhD studies of Safiah Zulkifli at Cranfield University. For the purposes of open access, the author has applied a Creative Commons Attribution (CC BY) licence to any Accepted Author Manuscript version arising from this submission.

Conflicts of Interest

The authors declare no conflicts of interest.

Data Availability Statement

Data supporting this study cannot be made available due to commercial restrictions.

References

1. R. Bartsch, J. Coyne, and K. Gray, *Drones in Society: Exploring the Strange New World of Unmanned Aircraft* (Routledge, 2016).

2. A. Foster, *The Pocket-Sized Drone Changing the Way the Military Operates* [Online] (cnet.com), accessed October 24, 2020, https://www.cnet.com/news/heres-the-tiny-drone-the-us-army-just-purchased-for-soldiers/.

3. C. J. Li and H. Ling, "An Investigation on the Radar Signatures of Small Consumer Drones," *IEEE Antennas and Wireless Propagation Letters* 16 (2017): 649–652, https://doi.org/10.1109/LAWP.2016.2594766.

4. J. S. Patel, F. Fioranelli, and D. Anderson, "Review of Radar Classification and RCS Characterisation Techniques for Small UAVs or Drones," *IET Radar, Sonar & Navigation* 12, no. 9 (2018): 911–919, https://doi.org/10.1049/iet-rsn.2018.0020.

5. S. Rahman and D. A. Robertson, "In-Flight RCS Measurements of Drones and Birds at K-Band and W-Band," *IET Radar, Sonar & Navigation* 13, no. 2 (2019): 300–309, https://doi.org/10.1049/iet-rsn.2018.5122.

6. M. Ritchie, F. Fioranelli, H. Griffiths, and B. Torvik, "Micro-Drone RCS Analysis," in *2015 IEEE Radar Conference* (2015), 452–456.

7. A. Balleri, "Measurements of the Radar Cross Section of a Nano-Drone at K-Band," in *2021 IEEE 8th International Workshop on Metrology for Aerospace (MetroAeroSpace)* (2021), 283–287.

8. I. Hinostroza, T. Letertre, and V. Mazières, "UAV Detection With K Band Embedded FMCW Radar," in *2017 Mediterranean Microwave Symposium (MMS)* (2017), 1–4.

9. Y. Kwag, I. Woo, H. Kwak, and Y. Jung, "Multi-Mode SDR Radar Platform for Small Air-Vehicle Drone Detection," in *2016 CIE International Conference on Radar (RADAR)* (2016), 1–4.

10. K. Stasiak, M. Ciesielski, A. Kurowska, and W. Przybysz, "A Study on Using Different Kinds of Continuous-Wave Radars Operating in C-Band for Drone Detection," in *2018 22nd International Microwave and Radar Conference (MIKON)* (2018), 521–526.

11. K. Stasiak and P. Samczynski, "FMCW Radar Implemented in SDR Architecture Using a USRP Device," in *2017 Signal Processing Symposium (SPSympo)* (2017), 1–5.

12. D. Gromek, M. Urbański, P. Krysik, P. Samczynski, A. Abramowicz, and K. Kulpa, "Two Channel Balanced RF FMCW Frontend for Radar Applications," in *2016 17th International Radar Symposium (IRS)* (2016), 1–5.

13. M. Caris, W. Johannes, S. Stanko, and N. Pohl, "Millimeter Wave Radar for Perimeter Surveillance and Detection of MAVs (Micro Aerial Vehicles)," in *2015 16th International Radar Symposium (IRS)* (2015), 284–287.

14. M. Caris, S. Stanko, W. Johannes, S. Sieger, and N. Pohl, "Detection and Tracking of Micro Aerial Vehicles With Millimeter Wave Radar," in *2016 European Radar Conference (EuRAD)* (2016), 406–408.

15. M. Caris, W. Johannes, S. Sieger, V. Port, and S. Stanko, "Detection of Small UAS With W-Band Radar," in *2017 18th International Radar Symposium (IRS)* (2017), 1–6.

16. J. Drozdowicz, M. Wielgo, P. Samczynski, et al., "35 GHz FMCW Drone Detection System," in *2016 17th International Radar Symposium (IRS)* (2016), 1–4.

17. A. Kyritsis, R. Makri, and N. Uzunoglu, "Detection of Low RCS Unmanned Air Systems Using K- Band Continuous Wave Doppler Radar," *Journal of Electrical and Computer Engineering* 2023 (2023): 13, https://doi.org/10.1155/2023/5683661.

18. J. Lee, M. Park, I. Eo, and B. Koo, "An X-Band FMCW Radar for Detection and Tracking of Miniaturized UAVs," in *2017 International Conference on Computational Science and Computational Intelligence (CSCI)* (2017), 1844–1845.

19. D. Shin, D. Jung, D. Kim, J. Ham, and S. Park, "A Distributed FMCW Radar System Based on Fiber-Optic Links for Small Drone Detection," *IEEE Transactions on Instrumentation and Measurement* 66, no. 2 (February 2017): 340–347, https://doi.org/10.1109/tim.2016.2626038.

20. S. Park and S. Park, "Configuration of an X-Band FMCW Radar Targeted for Drone Detection," in *2017 International Symposium on Antennas and Propagation (ISAP)* (2017), 1–2.

21. F. Ibañez Urzaiz, Á. Duque de Quevedo, J. Gismero Menoyo, and A. Asensio Lopez, "Design of Radio Frequency Subsystems of a Ubiquitous Radar in X Band," in *2017 International Carnahan Conference on Security Technology (ICCST)* (2017), 1–5.

22. A. Duque de Quevedo, F. Ibañez Urzaiz, J. Gismero Menoyo, and A. Asensio Lopez, "X-Band Ubiquitous Radar System: First Experimental Results," in *2017 International Carnahan Conference on Security Technology (ICCST)* (2017), 1–6.

23. F. I. Urzaiz, Á. D. de Quevedo, A. M. Ayuso, Á. G. Machado, J. G. Menoyo, and A. A. López, "Design, Implementation and First Experimental Results of an X-Band Ubiquitous Radar System," in *2018 IEEE Radar Conference (Radarconf18)* (2018), 1150–1155.

24. Á. D. De Quevedo, F. I. Urzaiz, J. G. Menoyo, and A. A. López, "Drone Detection and RCS Measurements With Ubiquitous Radar," in *2018 International Conference on Radar (RADAR)* (2018), 1–6.

25. Á. D. de Quevedo, F. I. Urzaiz, J. G. Menoyo, and A. A. López, "Remotely Piloted Aircraft Detection With Persistent Radar," in *2018 15th European Radar Conference (EuRAD)* (2018).

26. S. Engelbertz, C. Krebs, A. Küter, R. Herschel, R. Geschke, and D. Nüßler, "60 GHz Low Phase Noise Radar Front-End Design for the Detection of Micro Drones," in *2019 16th European Radar Conference (EuRAD)* (2019), 25–28.

27. A. Cidronali, M. Passafiume, P. Colantonio, et al., "System Level Analysis of Millimetre-Wave GaN-Based MIMO Radar for Detection of Micro Unmanned Aerial Vehicles," in *2019 Photonics & Electromagnetics Research Symposium—Spring (PIERS-Spring)* (2019), 438–450.

28. J. J. M. de Wit, R. I. A. Harmanny, and G. Prémel-Cabic, "Micro-Doppler Analysis of Small UAVs," in *2012 9th European Radar Conference* (2012), 210–213.

29. P. Molchanov, K. Egiazarian, J. Astola, R. I. A. Harmanny, and J. J. M. de Wit, "Classification of Small UAVs and Birds by Micro-Doppler Signatures," in *2013 European Radar Conference, Nuremberg* (2013), 172–175.

30. R. I. A. Harmanny, J. J. M. de Wit, and G. P. Cabic, "Radar micro-Doppler Feature Extraction Using the Spectrogram and the Cepstrogram," in *2014 11th European Radar Conference* (2014), 165–168.

31. J. J. M. de Wit, R. I. A. Harmanny, and P. Molchanov, "Radar Micro-Doppler Feature Extraction Using the Singular Value Decomposition," in *2014 International Radar Conference* (2014), 1–6.

32. S. Rahman and D. A. Robertson, "Radar Micro-Doppler Signatures of Drones and Birds at K-Band and W-Band," *Scientific Reports* 8, no. 1 (2018): 17396, https://doi.org/10.1038/s41598-018-35880-9.

33. A. Aldowesh, T. BinKhamis, T. Alnuaim, and A. Alzogaiby, "Low Power Digital Array Radar for Drone Detection and Micro-Doppler Classification," in *2019 Signal Processing Symposium (SPSympo)* (2019), 203–206.

34. S. Zulkifli and A. Balleri, "FMCW Radar Prototype Development for Detection and Classification of Nano-Targets," in *2020 IEEE International Radar Conference (RADAR)* (2020), 738–743.

35. S. Zulkifli and A. Balleri, "Design and Development of K-Band FMCW Radar for Nano-Drone Detection," in *2020 IEEE Radar Conference (Radarconf20)* (2020), 1–5.

36. Analog Devices, HMC739LP4 739LP4E—Analog [Online], accessed May 5, 2025, https://www.analog.com/media/en/technical-documentation/data-sheets/hmc739.pdf.

37. B. R. Mahafza, *Radar Systems Analysis and Design Using MATLAB*. 4th ed. (Chapman & Hall/CRC, 2022).

38. E. F. Knott, *Radar Cross Section Measurements* (Van Nostrand Reinhold, 1993).

39. S. Zulkifli, A. Corrias, and A. Balleri, "Detection of Flying Nano-Drone Signatures With a K-Band FMCW Radar," in *2024 IEEE International Workshop on Technologies for Defense and Security (Techdefense)* (2024), 278–282.



https://dspace.org/

A flexible Kband FMCW radar prototype for lowRCS nano drone detection

Zulkifli, Safiah; Balleri, Alessio

2025-12
Institution of Engineering and Technology (IET)
https://doi.org/10.1049/rsn2.70067
Zulkifli S, Balleri A. (2025) A flexible Kband FMCW radar prototype for lowRCS nanodrone detection. IET Radar, Sonar & Navigation, Volume 19, Issue 1, January/December 2025, Article number e70067

Downloaded from a DSpace repository. https://dspace.org/